



# Solar photocatalytic hydrogen production through metal sulfide/ UiO-66-NH<sub>2</sub> heterojunctions

Yilan Wang<sup>a,b</sup>, Lorena Gudiño<sup>a</sup>, Jorge Bedia<sup>a</sup>, Carolina Belver<sup>a,\*</sup>

<sup>a</sup> Chemical Engineering Department, Universidad Autonoma de Madrid, Campus Cantoblanco E-28049 Madrid, Spain

<sup>b</sup> Zhuhai-M.U.S.T. Science and Technology Research Institute, Guangdong, China

## ARTICLE INFO

### Keywords:

Photocatalysis  
Hydrogen production  
Heterojunction  
Metal organic framework  
Metal sulfide

## ABSTRACT

The design of efficient photocatalysts for hydrogen production by water electrolysis under solar irradiation still remains a challenge. Herein, a series of binary heterojunctions comprising metal sulfides and a zirconium-based MOF were synthesized and employed as photocatalysts for hydrogen production under simulated solar light using different scavengers. The highest hydrogen production rate ( $64.0 \mu\text{mol}\cdot\text{g}^{-1}\cdot\text{h}^{-1}$ ) was achieved using the CdS/UiO-66-NH<sub>2</sub> heterojunction under cocatalyst-free conditions and using TEOA as a hole scavenger. A synergistic effect between the CdS and the UiO-66-NH<sub>2</sub> was confirmed since the single semiconductors exhibited almost negligible hydrogen production. CdS/UiO-66-NH<sub>2</sub> characterization revealed that the improved photocatalytic performance was due to the formation of a Type II heterojunction among both semiconductors, thus favouring the separation of photogenerated electron-hole pairs. The findings of this study offer a novel perspective on the development of advanced MOF-based photocatalysts for hydrogen production under solar light.

## 1. Introduction

Hydrogen is characterized by a high energy density, providing more energy for the same volume of fuel than traditional fossil fuels, which together with its zero-emission characteristics positions it as an ideal alternative to conventional energy sources [1,2]. In the transport and industry sectors, hydrogen is regarded as a pivotal technology for achieving carbon neutrality [3,4]. However, to meet the escalating energy demands and promote the utilization of renewable sources, the efficient production and application of hydrogen have emerged as paramount challenges. In this context, photocatalytic hydrogen production has garnered extensive attention. By harnessing solar energy to achieve water decomposition, this technology demonstrates high efficiency and underlines its environmental friendliness, highlighting its inherent sustainability benefits [5,6].

Upon radiation exposure, the semiconductor photocatalyst undergoes electronic excitation, causing electrons to transition to the higher energy states of the conduction band and holes generation in the valence band. The excited electrons traverse within the photocatalyst and reach the surface, where they can reduce proton species and produce hydrogen, and at the same time the holes react with water

molecules or other species herein dissolved [7–9]. However, the efficiency and performance of this process are predominantly governed by the nature of the photocatalyst. A wide range of semiconductor types are currently under study, from conventional TiO<sub>2</sub> and its derivatives [8] to emerging ones, such as CdS [10], g-C<sub>3</sub>N<sub>4</sub> [11] or metal organic frameworks (MOFs) [12]. A meticulously designed proficient catalyst not only boosts reaction rates and selectivity but also mitigates energy consumption and enhances the stability of the reaction. Heterojunction formation using different functional materials in a single photocatalyst is among the strategies followed to achieve more efficient photocatalysts [13]. The heterojunction is defined as the interface between two different semiconductors with unequal band structures, which may lead to band alignment. This union may alter the electronic structure and light response performance, broadening light harvesting properties, improving chemical stability, enhancing the photoexcited charge separation, and thereby boosting photocatalytic hydrogen production [13,14].

Zr-, Zn- and Ti-MOFs have been among the most evaluated as photocatalysts [12]. UiO-66-NH<sub>2</sub> is emblematic of microporous MOFs, constituted by Zr<sub>6</sub>O<sub>4</sub>(OH)<sub>2</sub> metal nodes and the cyclic arrangement of the ligand 2-aminoterephthalic acid. It comprises tetrahedral and

\* Corresponding author.

E-mail address: [carolina.belver@uam.es](mailto:carolina.belver@uam.es) (C. Belver).

<https://doi.org/10.1016/j.seppur.2024.128663>

Received 23 April 2024; Received in revised form 20 June 2024; Accepted 1 July 2024

Available online 2 July 2024

1383-5866/© 2024 The Author(s). Published by Elsevier B.V. This is an open access article under the CC BY-NC-ND license (<http://creativecommons.org/licenses/by-nc-nd/4.0/>).

octahedral cages assembled periodically via triangular windows in a 1:2 ratio. Furthermore, owing to the inherent oxygen affinity of Zr(IV), the secondary structural units formed by Zr clusters exhibit inertness and structural stability under diverse chemical conditions [15–18]. Thus, UiO-66-NH<sub>2</sub> offers a combination of elevated surface area, tunable pore structures, and chemical robustness [19]. By other side, metal sulfides have attracted interest in recent decades due to their cost-effectiveness, excellent electrical conductivity, and outstanding performance in light response and electronic excitation. One of the main challenges of metal sulfides as photocatalysts is to achieve reasonable stability without compromising catalytic activity [20–22]. In this regard, heterojunction strategies have been proposed to enhance the stability of sulfide catalysts and mitigate their photo-corrosion tendencies. For instance, Tai et al. [23] fabricated a ternary CdS/Pt/MIL-125 photocatalyst. The distinctive ordered mesoporous structure, broadened light absorption range, increased active sites, enhanced light harvesting efficiency, and facilitated electron transfer all collectively contribute to the improved efficiency of hydrogen production. Mu et al. [24] engineered a Z-type heterostructure by decorating UiO-66-(COOH)<sub>2</sub>/ZnIn<sub>2</sub>S<sub>4</sub> with MoS<sub>2</sub> nanosheets. The intimate interfacial interactions among UiO-66-(COOH)<sub>2</sub>, MoS<sub>2</sub>, and ZnIn<sub>2</sub>S<sub>4</sub> facilitate the rapid transfer of photo-generated electrons, effectively promoting the photocatalytic reaction process.

This study aims to investigate the photocatalytic performance of novel metal sulfide/UiO-66-NH<sub>2</sub> heterojunctions for solar hydrogen production. Through a comprehensive exploration of different metal sulfides (namely CdS, Bi<sub>2</sub>S<sub>3</sub> and ZnS), we explore the synthesis of different heterojunctions to elucidate the effect of the metal sulfide nature on the properties and photocatalytic performance in their combination with UiO-66-NH<sub>2</sub>. Additionally, the photocatalytic mechanism will be proposed. The investigation seeks to provide insights into the distinctive photocatalytic capabilities and potential contributions to energy conversion presented by these heterojunctions.

## 2. Experimental

### 2.1. Reagents

Zirconium butoxide (Zr(OC<sub>4</sub>H<sub>9</sub>)<sub>4</sub>, 80 %), 2-aminoterephthalic acid (2ATA) (C<sub>8</sub>H<sub>7</sub>NO<sub>4</sub>, 99 %), formic acid (HCOOH, ≥ 95 %), cadmium sulfide (CdS, ≥ 99 %), bismuth sulfide (Bi<sub>2</sub>S<sub>3</sub>, ≥ 99 %), zinc sulfide (ZnS, ≥ 99 %), triethanolamine (TEOA, ≥ 99 %), sodium sulfide (Na<sub>2</sub>S·9H<sub>2</sub>O, ≥ 98 %), sodium sulfite (Na<sub>2</sub>SO<sub>3</sub>, pure grade), methanol (CH<sub>3</sub>OH, ≥ 99.9 %), were acquired from Sigma-Aldrich Corporation. N,N-dimethylformamide (C<sub>3</sub>H<sub>7</sub>NO, ≥ 99.8 %) was purchased from AppliChem. All these chemical reagents were of analytical grade and used without further purification.

### 2.2. Synthesis of UiO-66-NH<sub>2</sub>

The UiO-66-NH<sub>2</sub> was prepared via a solvothermal method with some modifications following previous work [25]. Briefly, zirconium precursor Zr(OC<sub>4</sub>H<sub>9</sub>)<sub>4</sub> (3.0 mmol) and organic linker 2ATA (3.0 mmol) were dissolved in formic acid (20 mL) and DMF solution (40 mL) at room temperature. The mixture was transferred in a Teflon-lined autoclave, sealed and placed in the oven at 120 °C for 24 h. The resulting samples were washed with DMF and methanol several times and further vacuum-dried at 70 °C overnight.

### 2.3. Synthesis of metal sulfide/UiO-66-NH<sub>2</sub> heterojunctions

0.25 g of commercial CdS or Bi<sub>2</sub>S<sub>3</sub> or ZnS were added to the zirconium and 2ATA mixture during the synthesis of UiO-66-NH<sub>2</sub>, thus favoring the growth of UiO-66-NH<sub>2</sub> over the metal sulfide. The synthesis methodology was the same above described, including the same washing and drying procedures. The resulting materials were named

CdS/UiO-66-NH<sub>2</sub>, Bi<sub>2</sub>S<sub>3</sub>/UiO-66-NH<sub>2</sub> and ZnS/UiO-66-NH<sub>2</sub>. For comparative purposes, the commercial metal sulfides were subjected to the same solvothermal treatment to verify their stability. Thus, 0.25 g of the metal sulfide was placed in a Teflon-lined autoclave containing 20 mL formic acid and 40 mL DMF. The materials were named CdS-, Bi<sub>2</sub>S<sub>3</sub>- and ZnS-blank.

### 2.4. Characterization of materials

X-ray diffraction (XRD) analyses were conducted in the 2θ range of 20 – 80° with a scan speed of 1.5° min<sup>−1</sup>, utilizing a Bruker D8 diffractometer equipped with Cu-Kα radiation (λ = 0.15406 nm). The textural characteristics were elucidated based on nitrogen adsorption–desorption isotherms at −196 °C obtained using a Micromeritics TriStar 123 instrument. The Brunauer-Emmett-Teller (BET) method was employed to determine the specific surface area (S<sub>BET</sub>), while the micropore volume (V<sub>MP</sub>) and the external or non-microporous surface area (S<sub>EXT</sub>) were established by the t-plot method. The total pore volume (V<sub>T</sub>) was derived from the nitrogen uptake at a relative pressure (P/P<sub>0</sub>) of 0.99. Prior to analysis, all specimens underwent a vacuum outgassing treatment at 120 °C for at least 4 h. UV–visible absorption spectra of the materials were acquired in the wavelength interval of 200 – 800 nm by using a Shimadzu 2501PC UV–vis spectrophotometer, calibrated with BaSO<sub>4</sub> as a reference. The registered reflectance spectra facilitated the determination of the band gap values through Tauc plot analysis, assuming an indirect semiconductor behavior. Scanning electron microscopy (SEM) analyses were conducted utilizing a Quanta 3D FEG system (FEI). Electron energy loss spectroscopy (EELS) studies in scanning transmission electron microscope (STEM) were performed in a Titan microscope (FEI) operating a low voltage (60 kV). Nyquist and Mott-Schottky plots were executed with a Metrohm Autolab potentiostat (PGSTAT204) connected to a flow cell suitable using three-electrode (DropSens ITO10) in a Faraday cage (Methrom). 1 mL of a dispersion, prepared by sonication of 10 mg of solid in 10 mL of 0.1 M Na<sub>2</sub>SO<sub>4</sub> solution, was dropped over electrochemical cell. At a fixed potential of −1.2 V, electrochemical impedance spectroscopy (EIS) was recorded from 10<sup>5</sup> to 0.1 Hz. The flat-band potential V<sub>fb</sub> of the material is derived from the Mott–Schottky equation [26]:

$$\frac{1}{C^2} = \frac{2}{\epsilon \cdot \epsilon_0 \cdot e \cdot N_D} \left( V - V_{fb} - \frac{k \cdot T}{e} \right) \left( \frac{1}{C^2} \right)^0 \rightarrow V_{fb} = V - \frac{k \cdot T}{e} \quad (1)$$

which C is the capacitance of the semiconductor-electrolyte junction at applied voltage V; ε and ε<sub>0</sub> are the permittivities of the semiconductor and the void, respectively; e is the electron charge (1.602·10<sup>−19</sup> J); k denotes the Boltzmann's constant (8.617·10<sup>−5</sup> eV·K<sup>−1</sup>); and T is the temperature (298 K). V<sub>fb</sub> is estimated from the intersection of the tangent with the abscissa in the plot of C<sup>−2</sup> vs applied potential (V). The determination of the conduction band (V<sub>CB</sub>) potential was relative to the normal hydrogen electrode (NHE) at pH 7, incorporating a Nernstian shift (equation (2) [27], considering the redox potential of Ag/AgCl (ΔV<sub>Ag/AgCl</sub> = 0.21 V) and the pH of the electrolyte as 6.8.

$$V_{CB} = V_{fb(Ag/AgCl, pH)} + \Delta V_{(Ag/AgCl : NHE)} - 0.059 \times (7 - pH) \quad (2)$$

The valence band potential (V<sub>VB</sub>) can be estimated based on bandgap value (E<sub>g</sub>) following Eq. (3).

$$V_{VB} = V_{CB} + E_g/e \quad (3)$$

### 2.5. Photocatalytic tests

The photocatalytic H<sub>2</sub> production was conducted within a 100 mL sealed glass reactor, covered with a borosilicate glass lid, and employing He as the carrier gas at a flow rate of 6.75 mL·min<sup>−1</sup>. This reactor was jacketed and linked to a Julabo CD-200F thermostatic bath, maintaining

the reaction temperature at 5 °C. The predetermined amount of photocatalyst ( $2 \text{ g} \cdot \text{L}^{-1}$ ) was dispersed in distilled water following the addition of a sacrificial agent. The optimal catalyst load was fixed and studied in a previous work [28]. The sacrificial agent concentration was fixed at 10 %vol. for TEOA, and at 0.1 M for the redox pair ( $\text{Na}_2\text{SO}_3/\text{Na}_2\text{S}$ ). After purging the mixture with He for 1 h, it underwent irradiation for 6 h using a solar simulator (SUNTEST® CPS + ) equipped with a 600 W NXE 1500B Xenon lamp and an ID 65 filter ( $\lambda > 320 \text{ nm}$ ).  $\text{H}_2$  sampling was carried out every 11 min in continuous online mode and analyzed using a Shimadzu gas chromatograph (GC-2030) equipped with a Barrier Discharge Ionization detector (BID). The GC utilized He as the carrier gas, with the detector set at 250 °C, and employed a Shimadzu capillary column with dimensions of 30 m length, 0.32 mm inner diameter, and operated at a temperature of 40 °C. Each experiment was conducted in duplicate, and the reported value represents the average. Furthermore, a long-term test was carried out to study the stability of the photocatalyst. The solution medium was recovered after the reaction and the total organic carbon was measured using Shimadzu TOC-L CSH equipment.

### 3. Result and discussion

#### 3.1. Characterization

All metal sulfide/ $\text{UiO-66-NH}_2$  heterojunctions and the respective single semiconductors underwent X-ray diffraction (XRD) analysis, depicted in Fig. 1. In the presence of formic acid and DMF solvent environment, commercial metal sulfides exhibited excellent stability without relevant changes in their crystalline structure. The XRD patterns of all heterostructures (Fig. 1) can overlay the original  $\text{UiO-66-NH}_2$  diffraction profile, establishing that the metal sulfide incorporation allows the successful crystallization of the MOF with its inherent crystalline structure. The intensity of the  $\text{UiO-66-NH}_2$  diffraction peaks, due to its crystallinity, means that the sulfide reflections were not clearly visible in any pattern, overlapping in most cases. Only the  $\text{ZnS}/\text{UiO-66-NH}_2$  (Fig. 1a) shows low-intensity peaks attributed to ZnS. Furthermore, scanning electron microscopy (SEM) analysis revealed that the  $\text{UiO-66-NH}_2$  crystallizes successfully in the presence of the metal sulfide, showing its characteristic octahedral morphology (Figure S1). After forming a heterojunction, the particle size slightly increased from 0.43 to 0.50  $\mu\text{m}$ . The morphology and particle size of both materials are characteristic of the  $\text{UiO-66-NH}_2$ , in the micron range. The presence of CdS does not alter these characteristics to any great extent.

The heterojunctions exhibit Type I nitrogen isotherms according to the IUPAC classification (Fig. 2a). Such characteristics of the isotherm assume a predominant microporous nature, further corroborated by the pore size distributions that established a bimodal distribution with pore sizes below 2 nm (Fig. 2b). Comparing the isotherms of the heterojunctions with the single semiconductors highlights their similarity with that of  $\text{UiO-66-NH}_2$  (Figure S2). This similarity corroborates the structural and morphological properties described above, mainly dominated by the  $\text{UiO-66-NH}_2$ . However, once the textural properties are established (summarized in Table 1), the reduction in both surface area and micropore volume caused by the presence of the metal sulfide can be observed. Thus, the metal sulfide blocks to some extent the porosity of the  $\text{UiO-66-NH}_2$ , despite which heterojunctions with high porosity and surface area are achieved.

Figure 3 and S3 illustrate the UV–Vis absorption spectra and the Tauc plots of all heterojunctions and the single semiconductors. The respective band gap values are collected in Table 1.  $\text{UiO-66-NH}_2$  is characterized by an absorption peak at 255 nm, that predominantly arises from the light absorption of the  $\text{Zr}_6$  clusters, accompanied by a second band at 325 nm attributed to the amine ligand light absorption [25,27]. Upon the heterojunction formation, a notable shift of the band edge towards longer wavelength values occurred in the  $\text{CdS}/\text{UiO-66-NH}_2$ , resulting in a noticeable low band gap value (Table 1), thus revealing the beneficial role of CdS in enhancing the light absorption capability. This effect was

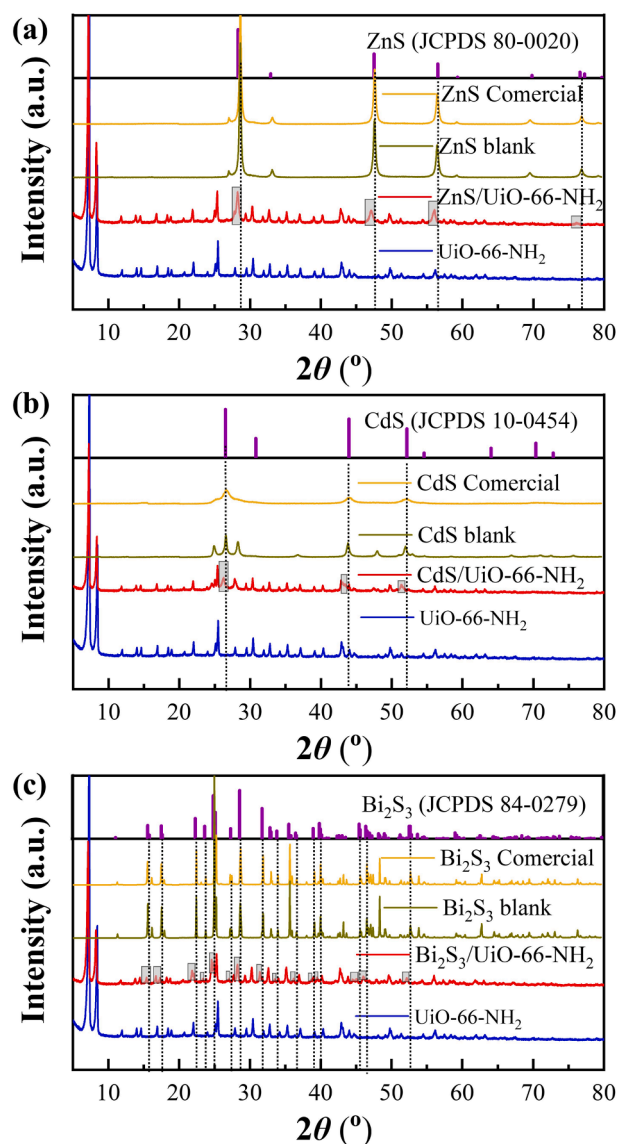


Fig. 1. XRD patterns of the synthesized heterojunctions and the single semiconductors: (a)  $\text{ZnS}/\text{UiO-66-NH}_2$ ; (b)  $\text{CdS}/\text{UiO-66-NH}_2$ ; and (c)  $\text{Bi}_2\text{S}_3/\text{UiO-66-NH}_2$ .

not observed in the other two heterojunctions.

Fig. 4a and b depict TEM images of  $\text{CdS}/\text{UiO-66-NH}_2$ , revealing a uniform dispersion of CdS nanoparticles on the surface of the octahedral  $\text{UiO-66-NH}_2$  particles. HRTEM was carried out to examine the surface interface between  $\text{UiO-66-NH}_2$  and CdS (Fig. 4c), the lattice spacing and corresponding Inverse Fast Fourier Transform patterns of 3.36 and 2.91 Å were observed, matching well with the (111) and (200) planes of CdS, respectively [29]. Furthermore, TEM and energy dispersive X-ray (EDX) analysis (Fig. 4d) were performed to investigate the elemental composition and spatial distribution of the  $\text{CdS}/\text{UiO-66-NH}_2$  heterojunction. The results of the EDX spectra confirm the presence of Zr, Cd, and S elements, and that the Cd and S elements are coated on the surface of  $\text{UiO-66-NH}_2$  evenly. These findings collectively validate the successful fabrication of the  $\text{CdS}/\text{UiO-66-NH}_2$  heterojunction.

#### 3.2. Photocatalytic $\text{H}_2$ production

Under simulated solar irradiation, the photocatalytic hydrogen production performance of the synthesized heterojunctions was investigated using triethanolamine (TEOA) as a hole scavenger in the absence

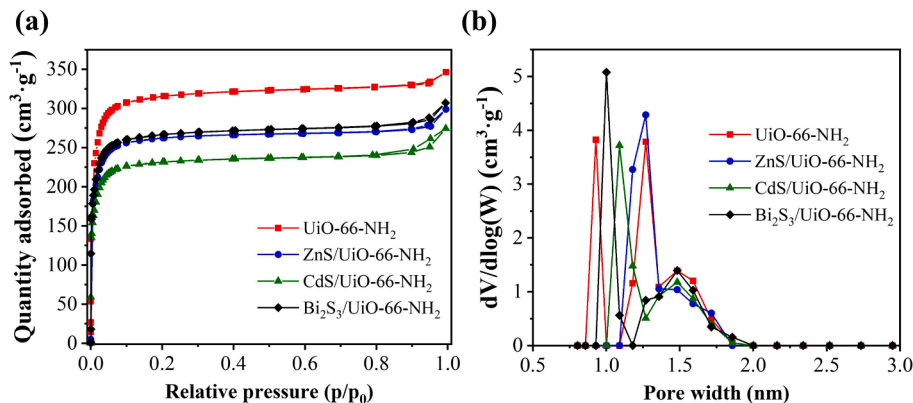


Fig. 2. (a) N<sub>2</sub> adsorption-desorption isotherms at -196 °C, and (b) DFT pore size distribution plots of all synthesized heterojunctions.

Table 1

Porous texture parameters and band gap values of the synthesized heterojunctions and the single semiconductors.

Sample	S <sub>BET</sub> (m <sup>2</sup> /g)	S <sub>EXT</sub> (m <sup>2</sup> /g)	V <sub>MP</sub> (cm <sup>3</sup> /g)	V <sub>T</sub> (cm <sup>3</sup> /g)	E <sub>g</sub> (eV)
UiO-66-NH <sub>2</sub>	1022	131	0.43	0.54	2.83
CdS	56	46	0.005	0.306	2.25
Bi <sub>2</sub> S <sub>3</sub>	—	—	—	—	1.17
ZnS	8	4	0.002	0.035	3.45
CdS/UiO-66-NH <sub>2</sub>	750	87	0.32	0.42	2.13
Bi <sub>2</sub> S <sub>3</sub> /UiO-66-NH <sub>2</sub>	864	110	0.36	0.48	2.90
ZnS/UiO-66-NH <sub>2</sub>	850	98	0.36	0.46	2.83

of additional co-catalysts, for 6 h. The observations revealed that both pristine UiO-66-NH<sub>2</sub> and Bi<sub>2</sub>S<sub>3</sub>/UiO-66-NH<sub>2</sub> exhibited negligible hydrogen production under simulated solar irradiation (Fig. 5a). ZnS/UiO-66-NH<sub>2</sub> displayed very weak hydrogen production, whereas the heterojunction CdS/UiO-66-NH<sub>2</sub> exhibited a hydrogen generation rate of 64.0 μmol·g<sup>-1</sup>·h<sup>-1</sup>. As shown in Fig. 5c, the hydrogen evolution rate of pure CdS was determined to be 8.0 μmol·g<sup>-1</sup>·h<sup>-1</sup>, indicating that the hydrogen production rate of the heterojunction was eight times higher than that of pure CdS. This suggests that the tight heterojunction formed between CdS and UiO-66-NH<sub>2</sub> enhances the photocatalytic performance. In contrast, the heterojunction formation between ZnS or Bi<sub>2</sub>S<sub>3</sub> and UiO-66-NH<sub>2</sub> did not significantly favour the hydrogen production rate (Fig. 5a), not even for ZnS (10.5 μmol·g<sup>-1</sup>·h<sup>-1</sup>) which shows similar activity to CdS (Fig. 5c and d), which can be attributed to an inefficient charge separation and movement between both semiconductors. As depicted in Fig. 5a, the hydrogen production rate of CdS/UiO-66-NH<sub>2</sub> gradually increased within the first 3 h under TEOA conditions, reaching a maximum at that time and accumulating nearly 80 μmol of hydrogen

within 6 h (Fig. 5b). The solution was recovered after the reaction and no change in pH was observed, which remained at a value of 11. The total organic carbon was also measured after reaction and no significant changes were observed, changing from 57 to 55 mg·L<sup>-1</sup>, due to the excess of TEOA used during the reaction. An additional test was carried out with a lower TEOA concentration, 0.1 M (not shown). The photocatalytic performance worsened compared with the test at 10 % TEOA. The H<sub>2</sub> production decreased from 64 to 19 μmol·g<sup>-1</sup>·h<sup>-1</sup> and accumulated hydrogen reduced from 80 to 22 μmol hydrogen within 6 h. The photocatalyst stability was determined by a 60 h long-term experiment (Figure S4). It is worth noting that the photocatalyst achieved the highest production rate during the first 10 h, after that the photocatalyst was deactivated and the hydrogen production decreased to reach a minimum production. The photocatalyst characterization after 60 h (Figure S2 and Table S1) reveals that the recovered material is just formed by CdS, showing the same UV-vis spectra and surface area, very low compared with the high porous network of the UiO-66-NH<sub>2</sub>. The same effect has been recently reported by authors [28], attributed to the high pH of the TEOA solution that attacks the MOF causing its transformation after long-term reaction times.

Using Na<sub>2</sub>S/Na<sub>2</sub>SO<sub>3</sub> as a hole scavenger all heterojunctions show a low hydrogen production, even CdS/UiO-66-NH<sub>2</sub> which only shows 6.9 μmol·g<sup>-1</sup>·h<sup>-1</sup> (Fig. 6a), accumulates 8.3 μmol of hydrogen within 6 h (Fig. 6b). Figure S6 shows the hydrogen production and accumulation of pure metal sulfides in the presence of Na<sub>2</sub>S/Na<sub>2</sub>SO<sub>3</sub> sacrificial agent. Although Na<sub>2</sub>S/Na<sub>2</sub>SO<sub>3</sub> is commonly used as a scavenger, providing dissolved sulfur ions (S<sup>2-</sup>) that act as reducing agents [30], its efficiency in this work is very low. TEOA has been described in the literature as both an electron donor and a capturer of photogenerated holes [31], thus maximizing the photocatalytic performance of the heterojunctions herein synthesized. The literature reports examples of other

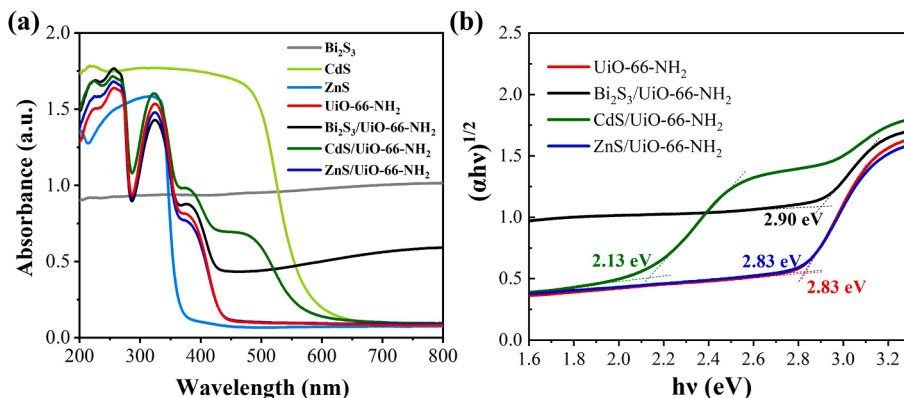
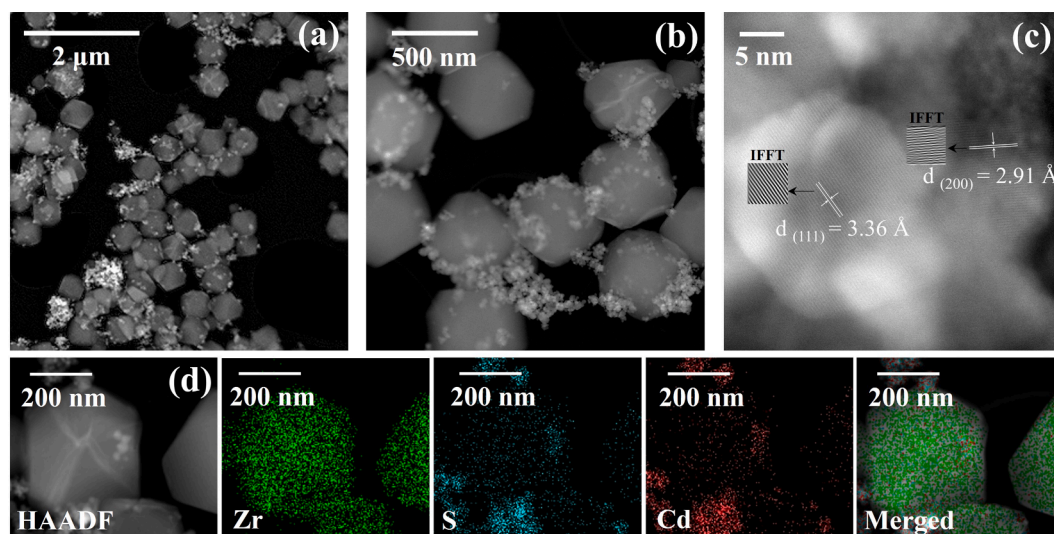
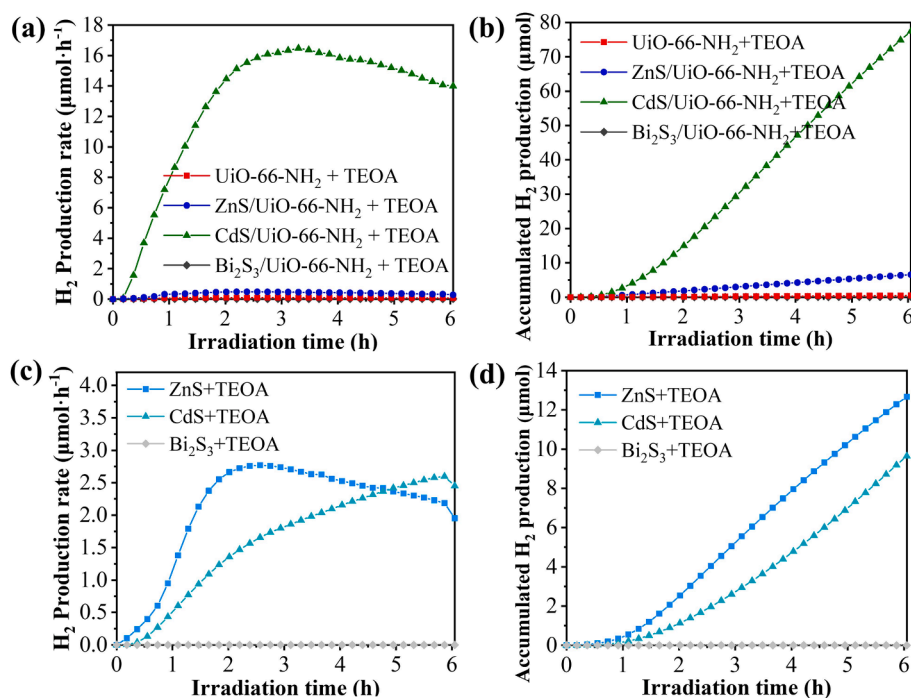


Fig. 3. (a) UV-vis diffuse absorbance spectra and (b) Tauc plots.





**Fig. 4.** (a,b) Transmission electron microscopy (TEM) images, (c) HRTEM image and IFFT (Inverse Fast Fourier Transform) patterns for (111) and (200) planes, (d) TEM and energy dispersive X-ray elemental mapping images of CdS/ UiO-66-NH<sub>2</sub>.



**Fig. 5.** (a) Hydrogen production and (b) accumulated H<sub>2</sub> production after 6 h over metal sulfide/UiO-66-NH<sub>2</sub> heterojunctions (photocatalyst dose = 2 g·L<sup>-1</sup>, scavenger concentration = 10 % TEOA). (c) Hydrogen production and (d) accumulated H<sub>2</sub> production after 6 h over metal sulfides with 10 % TEOA scavengers (temperature = 5 °C, light intensity = 600 W·m<sup>-2</sup>).

heterojunctions based on UiO-66-NH<sub>2</sub> for hydrogen production by photocatalysis summarized in Table 2. Among them, Zhang et al. [32] conducted hydrogen production using a ternary heterojunction WP/CdS/UiO-66 yielding a hydrogen production rate similar to ours, at 79 μmol·g<sup>-1</sup>·h<sup>-1</sup>. However, that work requires the incorporation of a third semiconductor (WP) to obtain a similar output as described herein. Hou et al. [33], Lian et al. [34], Dong et al. [35] and Wang et al. [36] achieved higher hydrogen production rates, even some reaching the magnitude of mmol·g<sup>-1</sup>·h<sup>-1</sup> by adding Pt salt in the water as a cocatalyst, which is costly for the process. Shanmugam et al. [37] also achieved a hydrogen production rate of 62.5 μmol·g<sup>-1</sup>·h<sup>-1</sup> using direct sunlight. Despite the differences, these studies collectively demonstrate the

potential of photocatalytic hydrogen technology, although special attention must be paid on photocatalyst stability during long-term experiments.

To evaluate the detailed electrochemical properties of the CdS/UiO-66-NH<sub>2</sub>, electrochemical impedance spectroscopy (EIS) was conducted resulting in the Nyquist plots shown in Fig. 7 for the CdS/UiO-66-NH<sub>2</sub> and the single conductors. The equivalent circuit model, shown in Fig. 7, fitted to the EIS data is R(RC). The high-frequency arc is related to the charge transfer at the cathode/electrolyte interface, and its diameter represents the value of the electrode's charge transfer resistance (R<sub>ct</sub>) [36,39]. The effective diameter of a semicircle could disclose the charge transfer resistance on the catalyst surface. As can be seen, the semicircle

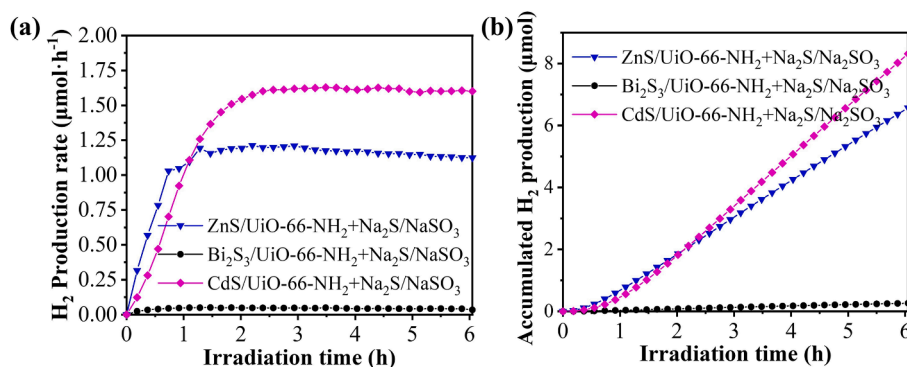


**Fig. 6.** (a) Hydrogen production and (b) accumulated H<sub>2</sub> production after 6 h over metal sulfide/UiO-66-NH<sub>2</sub> heterojunctions with 0.1 M Na<sub>2</sub>S/Na<sub>2</sub>SO<sub>3</sub> scavenger (temperature = 5 °C, light intensity = 600 W·m<sup>-2</sup>).

**Table 2**

Comparison of different photocatalysts and conditions for photocatalytic H<sub>2</sub> production.

Photocatalyst	Cocatalyst	Scavenger	Irradiation	Production (μmol·g <sup>-1</sup> ·h <sup>-1</sup> )	Ref.
WP/UiO-66/CdS	WP	lactic acid	Xe lamp λ > 420 nm	79	[32]
UiO-66-NH <sub>2</sub> @Au/CdS	Pt	L-ascorbic acid	Xe lamp λ > 420 nm	39.5	[33]
Pt@NH <sub>2</sub> -UiO-66/CdS	Pt	lactic acid	Xe lamp λ > 420 nm	37.8	[34]
UiO-66-NH <sub>2</sub> /COF	Pt	TEOA	Xe lamp λ > 420 nm	378	[35]
Pt@UiO-66-NH <sub>2</sub> @ZnIn <sub>2</sub> S <sub>4</sub>	Pt	benzylamine	Xe lamp λ > 420 nm	850	[36]
UiO-66-NH <sub>2</sub> /CuFe <sub>2</sub> O <sub>4</sub>	/	methanol	Real sunlight	62.5	[37]
MgIn <sub>2</sub> S <sub>4</sub> /UiO-66-NH <sub>2</sub>	/	methanol	Xe lamp λ > 420 nm	493.8	[38]
CdS/UiO-66-NH <sub>2</sub>	/	TEOA	Xe lamp-sunlight λ > 320 nm	64	this work

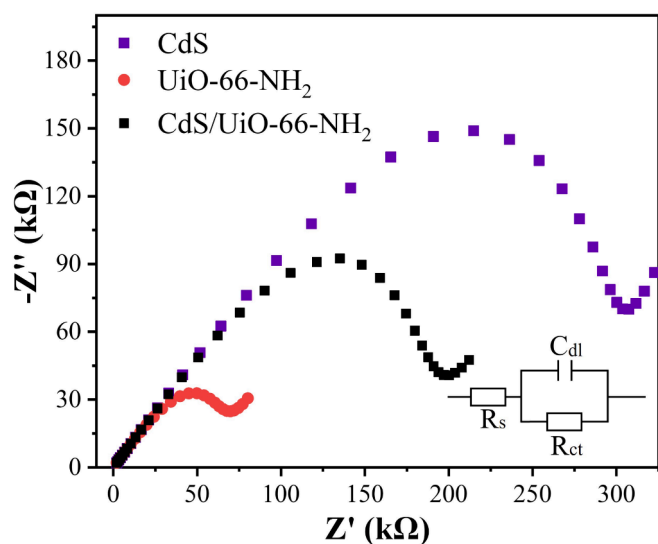


**Fig. 7.** Electrochemical impedance spectroscopy (EIS) Nyquist plots over the 10<sup>5</sup>–0.1 Hz frequency range in the dark.

of CdS/UiO-66-NH<sub>2</sub> lies within the CdS and the UiO-66-NH<sub>2</sub> indicating that the heterojunction has a stronger conductivity than the CdS but worse than the pristine MOF. Although the UiO-66-NH<sub>2</sub> shows better electrical conductivity its photocatalytic performance was really low, which can be attributed to its lower band gap and worse light absorption described before.

To understand and probe the origin of the catalytic performance of the heterojunction herein synthesized, the flat band potentials ( $V_{fb}$ ) of UiO-66-NH<sub>2</sub> and CdS were determined from the Mott-Schottky plots (Fig. 8). The positive slope of these plots indicates that both materials are n-type semiconductors. The x-intercepts at different frequencies yielded flat band potentials of  $-0.71$  and  $-0.87$  V for UiO-66-NH<sub>2</sub> and CdS, respectively. Consequently, the conduction band positions ( $V_{CB}$ ) of UiO-66-NH<sub>2</sub> and CdS were calculated to be  $-0.51$  and  $-0.67$  V, respectively. Additionally, the valence band potentials ( $V_{VB}$ ) were determined using the Equation (3). Based on these outcomes, Fig. 9 shows the heterojunction bands scheme conducting to the charge transfer mechanism characteristic of Type II heterojunction [40]. Under light irradiation, electrons and holes are generated in the CB and VB of both semiconductors, respectively. The heterojunction created enables the swift injection of photoexcited electrons from the CB of CdS into the CB of UiO-66-NH<sub>2</sub>. The energy of the CB of UiO-66-NH<sub>2</sub> meets the oxidation–reduction potential of  $H^+/H_2$ , thus proton-coupled reduction of water molecules occurs resulting in hydrogen generation [41]. Simultaneously, photogenerated holes from UiO-66-NH<sub>2</sub> transfer to the VB of CdS, thus the photogenerated  $e^-$  and  $h^+$  can move in opposite directions, leading to a spatial on different semiconductors and preventing their recombination. At the same time, TEOA molecules capture the photo-generated holes, favouring charge separation and the consequent reduction of the protons to generate hydrogen, which is similar to the heterojunction formed in other works [34,39]. Consequently, the enhanced H<sub>2</sub> generation performance of CdS/UiO-66-NH<sub>2</sub> can be attributed to the synergistic effect of CdS and UiO-66-NH<sub>2</sub>, which effectively accelerates the separation of carriers and promotes the reduction of  $H^+$ .

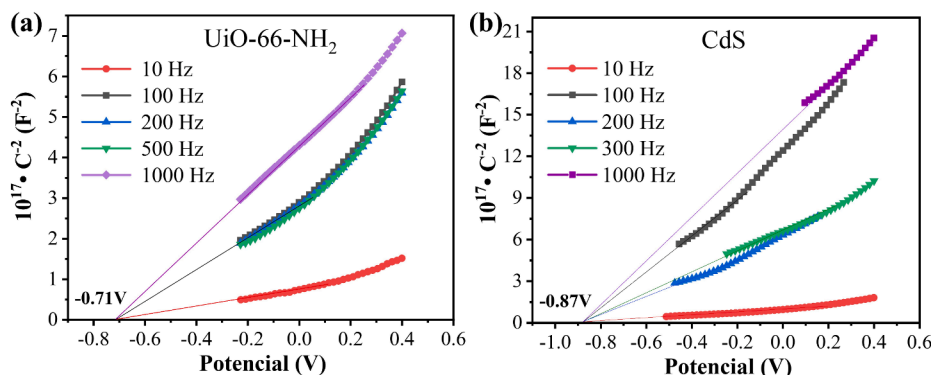


Fig. 8. Mott-Schottky plots of (a) UiO-66-NH<sub>2</sub> and (b) CdS.

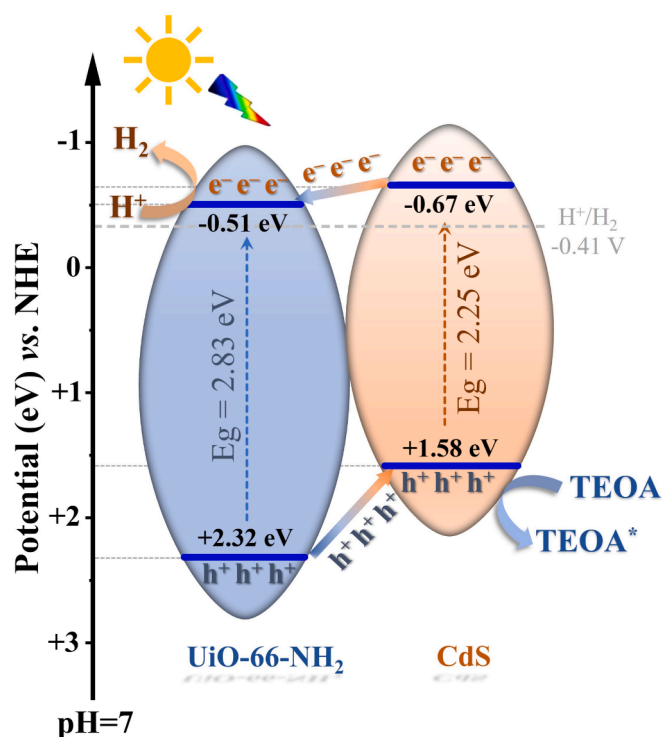


Fig. 9. Proposed mechanism for the enhanced H<sub>2</sub> production of the CdS/UiO-66-NH<sub>2</sub> heterojunction.

#### 4. Conclusion

In summary, a novel CdS/UiO-66-NH<sub>2</sub> heterojunction has been developed as photocatalyst for solar hydrogen production. By a common solvothermal way, improved photocatalytic performance was obtained due to the synergistic effect of CdS and UiO-66-NH<sub>2</sub>, yielding a Type II heterojunction. The optimal hydrogen generation rate of 64.0  $\mu\text{mol}\cdot\text{g}^{-1}\cdot\text{h}^{-1}$  was achieved under simulated solar light using TEOA as a hole scavenger. Other ZnS/UiO-66-NH<sub>2</sub> and Bi<sub>2</sub>S<sub>3</sub>/UiO-66-NH<sub>2</sub> heterojunctions were synthesized and studied, but their photocatalytic performance was almost negligible, similar to the single semiconductors, due to their poor light absorption properties. The notable improvement in the photocatalytic performance of the CdS/UiO-66-NH<sub>2</sub> heterojunction can be attributed to the efficient charge separation and transfer at the interface between CdS and UiO-66-NH<sub>2</sub>. However, the CdS/UiO-66-NH<sub>2</sub> heterojunction suffered deactivation after long-term operation times due to the MOF transformation, an important issue to be considered for potential applications of other heterojunctions based on UiO-66-NH<sub>2</sub>. Hence, this work may enrich the development of multi-

component photocatalysts for this technology.

#### CRediT authorship contribution statement

**Yilan Wang:** Writing – original draft, Methodology, Investigation, Conceptualization. **Lorena Gudiño:** Writing – original draft, Methodology, Investigation. **Jorge Bedia:** Writing – review & editing, Visualization, Validation, Supervision, Investigation, Funding acquisition, Conceptualization. **Carolina Belver:** Writing – review & editing, Visualization, Validation, Supervision, Project administration, Investigation, Funding acquisition, Conceptualization.

#### Declaration of competing interest

The authors declare that they have no known competing financial interests or personal relationships that could have appeared to influence the work reported in this paper.

#### Data availability

Data will be made available on request.

#### Acknowledgments

This work is deeply appreciative of the financial support provided by the Spanish State Research Agency and FSE + for funding (PID2022-141056OB-I00/MCIN/AEI/10.13039/501100011033; TED2021-129948B-I00). Yilan Wang is grateful for the scholarship support from the China Scholarship Council (CSC No. 201908610198). L. Gudiño thanks to Spanish MCI (FPI-PRE2020-093998 grant). The authors thank Shuai Zhang from the South China University of Technology (China) for invaluable assistance with SEM images. The authors are also grateful to the Research Support Services of the University of Extremadura (SAIUEX) and the Transmission electron microscopy area of the University of Zaragoza.

#### Appendix A. Supplementary data

Supplementary data to this article can be found online at <https://doi.org/10.1016/j.seppur.2024.128663>.

#### References

- [1] T. Longden, F.J. Beck, F. Jotzo, R. Andrews, M. Prasad, 'Clean' hydrogen? – Comparing the emissions and costs of fossil fuel versus renewable electricity based hydrogen, *Appl. Energy*. 306 (2022) 118145, <https://doi.org/10.1016/j.apenergy.2021.118145>.
- [2] H. Nazir, C. Louis, S. Jose, J. Prakash, N. Muthuswamy, M.E.M. Buan, C. Flox, S. Chavan, X. Shi, P. Kauranen, T. Kallio, G. Maia, K. Tammeveski, N. Lympieropoulos, E. Carcadea, E. Veziroglu, A. Iranzo, A.M. Kannan, Is the H<sub>2</sub> economy realizable in the foreseeable future? Part I: H<sub>2</sub> production methods, *Int. J.*

- Hydrogen Energy. 45 (2020) 13777–13788, <https://doi.org/10.1016/j.IJHYDENE.2020.03.092>.
- [3] A. Kovač, M. Paranos, D. Marciuš, Hydrogen in energy transition: A review, *Int. J. Hydrogen Energy*. 46 (2021) 10016–10035, <https://doi.org/10.1016/j.IJHYDENE.2020.11.256>.
  - [4] T. Capurso, M. Stefanizzi, M. Torresi, S.M. Camporeale, Perspective of the role of hydrogen in the 21st century energy transition, *Energy Convers. Manag.* 251 (2022) 114898, <https://doi.org/10.1016/j.ENCONMAN.2021.114898>.
  - [5] M. Ismael, A review and recent advances in solar-to-hydrogen energy conversion based on photocatalytic water splitting over doped-TiO<sub>2</sub> nanoparticles, *Sol. Energy*. 211 (2020) 522–546, <https://doi.org/10.1016/j.SOLENER.2020.09.073>.
  - [6] S.E. Hosseini, M.A. Wahid, Hydrogen from solar energy, a clean energy carrier from a sustainable source of energy, *Int. J. Energy Res.* 44 (2020) 4110–4131, <https://doi.org/10.1002/ER.4930>.
  - [7] P. Ganguly, M. Harb, Z. Cao, L. Cavallo, A. Breen, S. Dervin, D.D. Dionysiou, S. C. Pillai, 2D Nanomaterials for Photocatalytic Hydrogen Production, *ACS Energy Lett.* 4 (2019) 1687–1709, [https://doi.org/10.1021/ACSENERGYLETT.9B00940/ASSET/IMAGES/LARGE/NZ-2019-00940Y\\_0020.JPEG](https://doi.org/10.1021/ACSENERGYLETT.9B00940/ASSET/IMAGES/LARGE/NZ-2019-00940Y_0020.JPEG).
  - [8] V. Kumaravel, S. Mathew, J. Bartlett, S.C. Pillai, Photocatalytic hydrogen production using metal doped TiO<sub>2</sub>: A review of recent advances, *Appl. Catal. B Environ.* 244 (2019) 1021–1064, <https://doi.org/10.1016/j.APCATB.2018.11.080>.
  - [9] C.Y. Toe, C. Tsounis, J. Zhang, H. Masood, D. Gunawan, J. Scott, R. Amal, Advancing photoreforming of organics: highlights on photocatalyst and system designs for selective oxidation reactions, *Energy Environ. Sci.* 14 (2021) 1140–1175, <https://doi.org/10.1039/D0EE03116J>.
  - [10] C.M. Wolff, P.D. Frischmann, M. Schulze, B.J. Bohn, R. Wein, P. Livadas, M. T. Carlson, F. Jäckel, J. Feldmann, F. Würthner, J.K. Stolarczyk, All-in-one visible-light-driven water splitting by combining nanoparticulate and molecular co-catalysts on CdS nanorods, *Nat. Energy* 3 (2018) 862–869, <https://doi.org/10.1038/s41560-018-0229-6>.
  - [11] V. Kumaravel, M.D. Imam, A. Badreldin, R.K. Chava, J.Y. Do, M. Kang, A. Abdel-Wahab, Photocatalytic Hydrogen Production: Role of Sacrificial Reagents on the Activity of Oxide, Carbon, and Sulfide Catalysts, *Catalysts*. 9 (2019) 276, <https://doi.org/10.3390/CATAL9030276>.
  - [12] Y.C. Wang, X.Y. Liu, X.X. Wang, M.S. Cao, Metal-organic frameworks based photocatalysts: Architecture strategies for efficient solar energy conversion, *Chem. Eng. J.* 419 (2021) 129459, <https://doi.org/10.1016/j.CEJ.2021.129459>.
  - [13] K. Afroz, M. Moniruddin, N. Bakranov, S. Kudaibergenov, N. Nuraje, A heterojunction strategy to improve the visible light sensitive water splitting performance of photocatalytic materials, *J. Mater. Chem. A*. 6 (2018) 21696–21718, <https://doi.org/10.1039/C8TA04165B>.
  - [14] H. Wang, L. Zhang, Z. Chen, J. Hu, S. Li, Z. Wang, J. Liu, X. Wang, Semiconductor heterojunction photocatalysts: Design, construction, and photocatalytic performances, *Chem. Soc. Rev.* 43 (2014) 5234–5244, <https://doi.org/10.1039/c4cs00126e>.
  - [15] D. Zou, D. Liu, Understanding the modifications and applications of highly stable porous frameworks via UiO-66, *Mater. Today Chem.* 12 (2019) 139–165, <https://doi.org/10.1016/j.MTCHM.2018.12.004>.
  - [16] R. Wang, L. Liu, S. Subhan, Y. Muhammad, Y. Hu, M. Huang, Y. Peng, Z. Zhao, Z. Zhao, Engineering pH-switchable UiO-66 via in-situ amino acid doping for highly selective adsorption of anionic dyes, *Chem. Eng. J.* 395 (2020) 124958, <https://doi.org/10.1016/j.CEJ.2020.124958>.
  - [17] P. Hu, R. Wang, Z. Gao, S. Jiang, Z. Zhao, H. Ji, Z. Zhao, Improved interface compatibility of hollow H-Zr<sub>0.1</sub>Ti<sub>0.9</sub>O<sub>2</sub> with UiO-66-NH<sub>2</sub> via Zr-Ti bidirectional penetration to boost visible photocatalytic activity for acetaldehyde degradation under high humidity, *Appl. Catal. B Environ.* 296 (2021) 120371, <https://doi.org/10.1016/j.APCATB.2021.120371>.
  - [18] Q. Yang, Q. Xu, H.L. Jiang, Metal-organic frameworks meet metal nanoparticles: synergistic effect for enhanced catalysis, *Chem. Soc. Rev.* 46 (2017) 4774–4808, <https://doi.org/10.1039/C6CS00724D>.
  - [19] Y. Shi, A.F. Yang, C.S. Cao, B. Zhao, Applications of MOFs: Recent advances in photocatalytic hydrogen production from water, *Coord. Chem. Rev.* 390 (2019) 50–75, <https://doi.org/10.1016/j.CCR.2019.03.012>.
  - [20] G. Zhang, Z. Guan, J. Yang, Q. Li, Y. Zhou, Metal Sulfides for Photocatalytic Hydrogen Production: Current Development and Future, *Challenges* 2200587 (2022) 1–15, <https://doi.org/10.1002/solr.202200587>.
  - [21] N. Photocatalytic, S.L. Lee, C. Chang, Recent Progress on Metal Sulfide Composite Hydrogen Production, *Catalysts* 9 (2019) 457, <https://doi.org/10.3390/catal9050457>.
  - [22] Z. Mamiyev, N.O. Balayeva, Metal Sulfide Photocatalysts for Hydrogen Generation: A Review of Recent, *Advances, Catalysts* 12 (2022) 1–36, <https://doi.org/10.3390/catal12111316>.
  - [23] C. Tai, H. Liu, Y. Hu, Fabrication of CdS/Pt/MIL-125 with Effective Spatial Separation for Improved Visible-Light Catalytic H<sub>2</sub> Evolution Using γ-Ray Irradiation, *ACS Sustain. Chem. Eng.* 8 (2020) 18196–18205, [https://doi.org/10.1021/ACSSUSCHEMENG.0C06598/SUPPL\\_FILE/SC0C06598\\_SI\\_001.PDF](https://doi.org/10.1021/ACSSUSCHEMENG.0C06598/SUPPL_FILE/SC0C06598_SI_001.PDF).
  - [24] F. Mu, Q. Cai, H. Hu, J. Wang, Y. Wang, S. Zhou, Y. Kong, Construction of 3D hierarchical microarchitectures of Z-scheme UiO-66-(COOH)<sub>2</sub>/ZnIn<sub>2</sub>S<sub>4</sub> hybrid decorated with non-noble MoS<sub>2</sub> cocatalyst: A highly efficient photocatalyst for hydrogen evolution and Cr(VI) reduction, *Chem. Eng. J.* 384 (2020) 123352, <https://doi.org/10.1016/j.CEJ.2019.123352>.
  - [25] Y.L. Wang, M. Peñas-Garzón, J.J. Rodríguez, J. Bedia, C. Belver, Enhanced photodegradation of acetaminophen over Sr@TiO<sub>2</sub>/UiO-66-NH<sub>2</sub> heterostructures under solar light irradiation, *Chem. Eng. J.* 446 (2022) 137229, <https://doi.org/10.1016/j.cej.2022.137229>.
  - [26] C. Baumanis, D.W. Bahnemann, TiO<sub>2</sub> Thin Film Electrodes: Correlation between Photocatalytic Activity and Electrochemical Properties, *J. Phys. Chem. C*. 112 (2008) 19097–19101, <https://doi.org/10.1021/JP807655A>.
  - [27] M. Peñas-Garzón, M.J. Sampaio, Y.L. Wang, J. Bedia, J.J. Rodríguez, C. Belver, C. G. Silva, J.L. Faria, Solar photocatalytic degradation of parabens using UiO-66-NH<sub>2</sub>, *Sep. Purif. Technol.* 286 (2022), <https://doi.org/10.1016/j.seppur.2022.120467>.
  - [28] L. Gudiño, M. Peñas-Garzón, J.J. Rodríguez, J. Bedia, C. Belver, Photochemical transformation of UiO-66-NH<sub>2</sub> during hydrogen Generation under solar irradiation, *Cat. Comm.* 187 (2024) 106858, <https://doi.org/10.1016/j.catcom.2024.106858>.
  - [29] J. Zhao, H. Yang, Y. Li, K. Lu, Photocatalytic activity of CdS nanoparticles enhanced by the interaction between piezotronic effect and phase junction, *J. Alloys Compd.* 815 (2020) 152494, <https://doi.org/10.1016/J.JALLCOM.2019.152494>.
  - [30] C. Xia, C. Xue, W. Bian, J. Liu, J. Wang, Y. Wei, J. Zhang, Hollow Co<sub>9</sub>S<sub>8</sub>/CdS Nanocages as Efficient Photocatalysts for Hydrogen Evolution, *ACS Appl. Nano Mater.* 4 (2021) 2743–2751, [https://doi.org/10.1021/ACSANM.0C03389/SUPPL\\_FILE/ANOC03389\\_SI\\_001.PDF](https://doi.org/10.1021/ACSANM.0C03389/SUPPL_FILE/ANOC03389_SI_001.PDF).
  - [31] N. Güy, Directional transfer of photocarriers on CdS/g-C<sub>3</sub>N<sub>4</sub> heterojunction modified with Pd as a cocatalyst for synergistically enhanced photocatalytic hydrogen production, *Appl. Surf. Sci.* 522 (2020) 146442, <https://doi.org/10.1016/J.APSUSC.2020.146442>.
  - [32] Y. Zhang, Z. Jin, Effective electron-hole separation over a controllably constructed WP/UiO-66/CdS heterojunction to achieve efficiently improved visible-light-driven photocatalytic hydrogen evolution, *Phys. Chem. Chem. Phys.* 21 (2019) 8326–8341, <https://doi.org/10.1039/c9cp01180c>.
  - [33] X. Hou, L. Wu, L. Gu, G. Xu, H. Du, Y. Yuan, Maximizing the photocatalytic hydrogen evolution of Z-scheme UiO-66-NH<sub>2</sub>@Au/CdS by aminated-functionalized linkers, *J. Mater. Sci. Mater. Electron.* 30 (2019) 5203–5211, <https://doi.org/10.1007/S10854-019-00819-X/SCHEMES/1>.
  - [34] Z. Lian, Z. Li, F. Wu, Y. Zhong, Y. Liu, W. Wang, J. Zi, W. Yang, Photogenerated hole traps in metal-organic-framework photocatalysts for visible-light-driven hydrogen evolution, *Commun. Chem.* 51 (5) (2022) 1–8, <https://doi.org/10.1038/s42004-022-00713-4>.
  - [35] S. Dong, X. Liu, X. Kong, F. Dong, Y. Yu, L. Wang, D. Wang, Z. He, S. Song, Boosting photocatalytic H<sub>2</sub> evolution on UiO-66-NH<sub>2</sub>/covalent triazine-based frameworks composites by constructing a covalent heterojunction, *Environ. Sci. Pollut. Res.* 30 (2023) 111039–111050, <https://doi.org/10.1007/s11356-023-30258-5>.
  - [36] L. Wang, Y. Zhao, B. Zhang, G. Wu, J. Wu, H. Hou, Spatial separation of redox centers for boosting cooperative photocatalytic hydrogen evolution with oxidation coupling of benzylamine over Pt@UiO-66-NH<sub>2</sub>/ZnIn<sub>2</sub>S<sub>4</sub>, *Catal. Sci. Technol.* 13 (2023) 2517–2528, <https://doi.org/10.1039/D3CY00089C>.
  - [37] M. Shanmugam, N. Agamendran, K. Sekar, Efficient Charge Transfer of p-n Heterojunction UiO-66-NH<sub>2</sub>/CuFe<sub>2</sub>O<sub>4</sub> Composite for Photocatalytic Hydrogen Production, *Catalysts*. 14 (2024) 341, <https://doi.org/10.3390/catal14060341>.
  - [38] S.P. Tripathy, S. Subudhi, A. Ray, P. Behera, G. Swain, M. Chakraborty, K. Parida, MgIn<sub>2</sub>S<sub>4</sub>/UiO-66-NH<sub>2</sub> MOF-based heterostructure: Visible-light-responsive Z-scheme-mediated synergistically enhanced photocatalytic performance toward hydrogen and oxygen evolution, *Langmuir*. 39 (2023) 7294–7306, <https://doi.org/10.1021/acs.langmuir.3c00151>.
  - [39] H. Zhang, Z. Yu, R. Jiang, Y. Hou, J. Huang, H. Zhu, F. Yang, M. Li, F. Li, Q. Ran, Metal organic frameworks constructed heterojunction with α-NiS-β-NiS/CdS: The effect of organic-ligand in UiO-66 for charge transfer of photocatalytic hydrogen evolution, *Renew. Energy*. 168 (2021) 1112–1121, <https://doi.org/10.1016/J.RENENE.2020.12.102>.
  - [40] Y. Wang, Q. Wang, X. Zhan, F. Wang, M. Safdar, J. He, Visible light driven type II heterostructures and their enhanced photocatalysis properties: a review, *Nanoscale*. 5 (2013) 8326–8339, <https://doi.org/10.1039/C3NR01577G>.
  - [41] B. Liang, N. Zhang, C. Chen, X. Liu, R. Ma, S. Tong, Z. Mei, V.A.L. Roy, H. Wang, Y. Tang, Hierarchical yolk-shell layered potassium niobate for tuned pH-dependent photocatalytic H<sub>2</sub> evolution, *Catal. Sci. Technol.* 7 (2017) 1000–1005, <https://doi.org/10.1039/c6cy02640k>.